Hindawi
International Transactions on Electrical Energy Systems
Volume 2022, Article ID 5059215, 19 pages
https://doi.org/10.1155/2022/5059215

Research Article

A Novel Controller Design for Small-Scale Islanded Microgrid Integrated with Electric Vehicle-Based Energy Storage Management

Nihal Omar, Anil Kumar Tiwari, K. Seethalekshmi, and Nitin Anand Shrivastava

Department of Electrical Engineering, Institute of Engineering and Technology, Lucknow 226021, UP, India

Correspondence should be addressed to K. Seethalekshmi; seethalekshmik@ietlucknow.ac.in and Nitin Anand Shrivastava; nitinshrivastava@ietlucknow.ac.in

Received 4 February 2022; Accepted 28 March 2022; Published 29 April 2022

Academic Editor: Kamran Iqbal

Small-scale islanded microgrid technology has the potential to utilize renewable sources for electrification in extreme areas where conventional transmission of power is difficult. But due to the absence of a utility grid in the islanded operation, voltage and frequency control becomes the major concern. Instead of using a centralized large battery storage system, electric vehicle- (EV-) based distributed energy storage may provide a dynamic and much cheaper energy storage solution for small-scale systems in the long run. The only issue is to effectively manage the dynamics of EV penetration for achieving the overall control in the islanded system. To address the same issue, this paper proposes a novel segregation-based inverter control structure for an islanded microgrid while employing EVs as an energy storage system, thus eliminating the need for centralized storage. The designed integrated control structure simultaneously attends to the voltage and frequency regulation need of the system, overcoming the issue of control lag, along with energy storage and management aspects in the microgrid operation for controlling the power flow under various practical scenarios. Extensive experimental studies are performed in MATLAB/SIMULINK environment, which indicates that the proposed integrated control structure gives a satisfactory performance under various scenarios encompassing load variation, renewable energy uncertainties, and EV dynamics in comparison with conventional control schemes employed in the islanded microgrid.

1. Introduction

The major problem with renewable energy sources (RES) is their intermittent and unpredictable nature. So to utilize RES, a large and complex control is required. For electrification of remote rural areas, the islanded system is essentially required [1–4]. RES-based microgrid (MG) requires a power electronics-based converter in the system; thus, it may adversely affect the overall power quality of the system. Further, any islanded MG itself suffers from the lack of system inertia because RES are integrated through power electronic controllers, which gets manifested into issues in frequency regulation [5–7]. Having an integrated DC bus in the system may improve this issue a little bit.

The proper functioning of an MG includes complete control of the system under load variations, system disturbances, profile variation, connection or disconnection status of the RES, proper energy storage and management (ESM) in the system, voltage maintenance, frequency regulation, and also ensuring good power quality. Thus, energy storage is used in MG [8, 9]. The use of electric vehicles (EVs) in MG for ESM is a promising area of research because of its fast charging and discharging capabilities. The bidirectional power flow in EV is called vehicle-to-grid (V2G) for discharging operation and grid-to-vehicle (G2V) for charging operation of the vehicle [10, 11].

The inverter control is essential in MG for its proper functioning and operation [12, 13]. However, the reported work in [12, 13] does not consider the integration of RES and EVs. As the system starts including more and more intrinsic mechanisms and also approaches towards more practical scenarios, conventional control starts failing to operate.

To overcome this, various papers have investigated the functioning of MG with RES [5, 14–17], energy storage systems [18–20], some advanced ESM strategies designed with dynamic programming [21] and use of EVs in charging stations and V2G design [22–29]. A few works are reported in advanced inverter control structures like adaptive droop control [10, 30], proportional-integral (PI) controller [4], fuzzy logic [20, 31, 32], model predictive controllers [33] for MG control, and so on. In [31, 34–38], nonconventional optimization algorithms, genetic algorithms, butterfly optimization, and so on are applied to tune the controllers. These control techniques are effective and adaptive; however, they require a lot of iterative computational memory which may create hurdles in real-time operation and are prone to be stuck at local optimum [39, 40]. This can generate an unintentional control lag that may hinder the controller from working at its global optimum operation.

With this background, the main problem, which is considered in this research, is to make the MG independent from centralized storage, external inertia support, and its control being free from the iterative computation. Most of the reported literature considers grid support or large-battery storage system (LBSS) [18, 30, 33] support for stabilizing the system. Some of the works consider only unidirectional power flow for EV charging stations [23–27, 29]. Reheat turbine system support and approximated solar and EV models are considered in [31] without including their intrinsic characteristics. None of these works has explored a standalone MG system with renewable generation and EV integration without the support of a power grid, LBSS, and turbine systems. Also, the nonlinearity of converters interfacing RES and EVs is avoided in most of the studies just by replacement from a first-order transfer function [39–41] to avoid certain complexities. This became the motivation for this work to include the same in the study.

A novel self-adaptive segregation-based inverter control (SBIC) with a dynamic band margin- (DBM-) based hysteresis controller, which uses the voltage signals for generating pulse width modulation (PWM) signals, is designed. Controller derives its adaptive features, through the segregation of its dynamic and fundamental components, of feedback. The main advantage of using SBIC is that it occupies very little memory, produces no control lag due to coordination delay, and is neither prone to be stuck at local optimum as the controller is not driven from an iterative algorithm or member function-based strategy. A proportional-resonant (PR) controller is used for high speed and improved steady-state performance. Also, bidirectional converters are designed for EV charging and discharging with small modifications controlled from an ESM scheme.

The major research contributions of this paper are as follows:

(i) Voltage and frequency regulation of islanded microgrid through EVs (using as energy storage) without any LBSS or external inertia support.

(ii) A novel, self-adaptive discrete sample coordinated SBIC scheme to overcome the problem of control lag which occurs due to complex computational techniques.

(iii) Consideration of intrinsic mechanisms and nonlinear characteristics of converters interfacing RES and EVs in the study.

(iv) Seamless coordination among proposed SBIC module, converter interfaced renewable generation and EV control module, and ESM module.

The outline of this paper is as follows. Section 2 discusses the detailed description of MG system modeling used for problem formulation. Section 3 consists of a detailed discussion over the proposed inverter control strategy and ESM strategy. Section 4 shows the simulation results and discussion over considered case scenarios. Finally, Section 5 provides conclusions.

2. System Modeling

The schematic of islanded MG system is shown in Figure 1. MG consists of a DC bus, integrated with RES, and an AC bus which is connected to the load. An inverter filter interface is used to connect both buses. The inverter used is a grid forming voltage source inverter, for isolated MG operations. EV modules are integrated at both DC and AC buses. The proposed main inverter controller and ESM algorithm module are shown with input and output signals for overall control and proper functioning of MG.

2.1. Renewable Generation Integration. RES (solar and wind) are integrated into the DC bus of the microgrid. Mathematical modeling and respective control mechanisms of solar and wind plants, connected to the DC bus, are detailed in this section.

2.1.1. Solar Plant. The solar power plant is integrated into the DC bus of a microgrid by the means of a boost converter that is being controlled by the incremental conductance maximum power point tracking (IC-MPPT) control algorithm. For dynamic modeling of PV array, a panel of 10 series modules and 47 parallel strings is chosen. Mathematical modeling of solar PV characteristics is reported in [5, 17].

Mathematically, IC-MPPT can be described in both discrete sample systems (DSS) and continuous differential systems (CDS), as shown in (1)–(7).

$$P(j) = P(j+1) - P(j), P(j) = V_j * I_j, \tag{1}$$

$$\sum_{j=1}^{n} P(j) = V_n * I_n - V_1 * I_1 = 0, \tag{2}$$

$$\sum_{j=1}^{n} P(j) = \sum_{j=1}^{k} P(j) + \sum_{j=k+1}^{n} P(j) = 0, \tag{3}$$

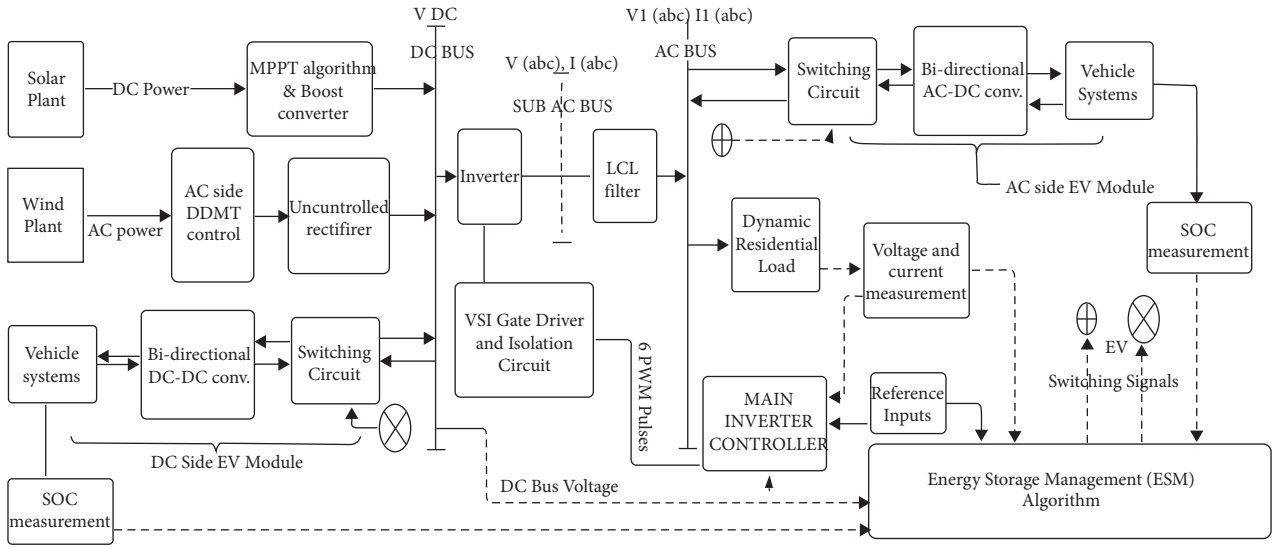

Figure 1: Schematic of the proposed microgrid system.

$$\sum_{j=1}^{k} P(j) = -\sum_{j=k+1}^{n} P(j). \tag{4}$$

In CDS, the derivative approach is used to find out the condition for the point of maximum power (PMP), as shown in (5) and (6). The condition of PMP in CDS is given in (7).

$$P = V * I, \tag{5}$$

$$\frac{\partial P}{\partial V} = I + V\frac{\partial I}{\partial V} = 0, \tag{6}$$

$$\frac{\partial V}{V} = -\frac{\partial I}{I}. \tag{7}$$

2.1.2. Wind Plant. The permanent magnet synchronous generator (PMSG) based wind power plant is integrated into the DC bus with the help of differential drive mass train (DDMT) control [15] and with an uncontrolled rectifier circuit. Mathematical modeling of the wind power plant is reported in [31]. DDMT control is a gearbox-based shaft speed control, a schematic diagram of which is shown in Figure 2. Mathematical modeling is shown in (8)–(11).

$$P = \omega_r T_s = \omega T_m, \tag{8}$$

$$2H_t\frac{d\omega}{dt} = T_m - T_s, \tag{9}$$

$$\frac{1}{\omega_{es}}\frac{d\theta_{sa}}{dt} = \omega - \omega_r, \tag{10}$$

$$T_s = K_s\theta_{sa} + D_t\frac{d\theta_{sa}}{dt}. \tag{11}$$

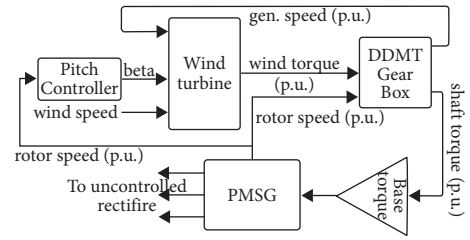

Figure 2: Schematic diagram of DDMT control.

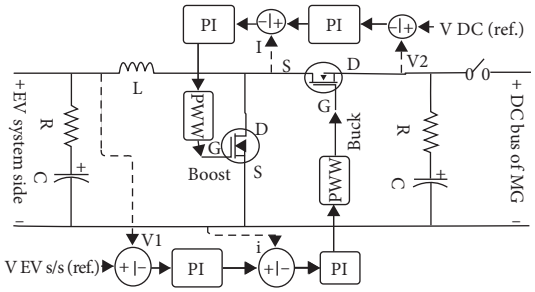

Figure 3: Schematic of bidirectional DC-DC converter with control.

2.2. Electric Vehicle (EV) Integration. In MG operation, EV modules are utilized as flexible loads for ESM and power flow maintenance and regulation of MG system via V2G and G2V operations [42]. During these operations, EV converter modules are in operation; hence, the design process focuses on the same. Converter and its control design affect the V2G and G2V process for both DC and AC sides of the MG. Some advanced converter designs are described in [27, 43].

2.2.1. Converter Design for DC Side EV System. DC side EV system modules are integrated into the DC bus of the MG with the help of a common bidirectional DC↔DC

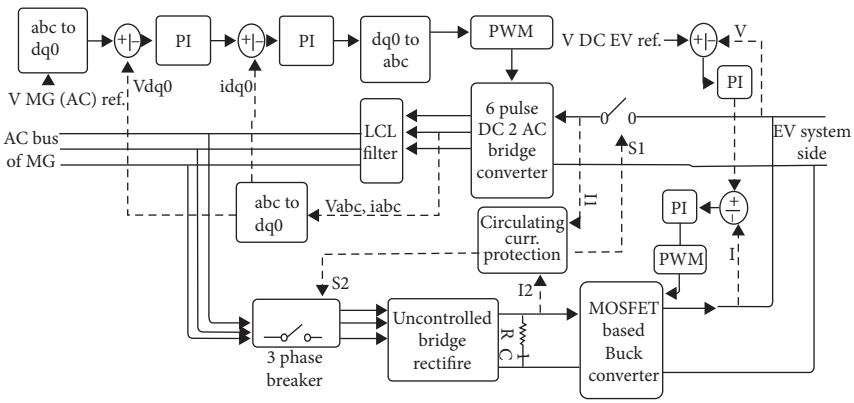

Figure 4: Schematic of designed bidirectional AC-DC converter.

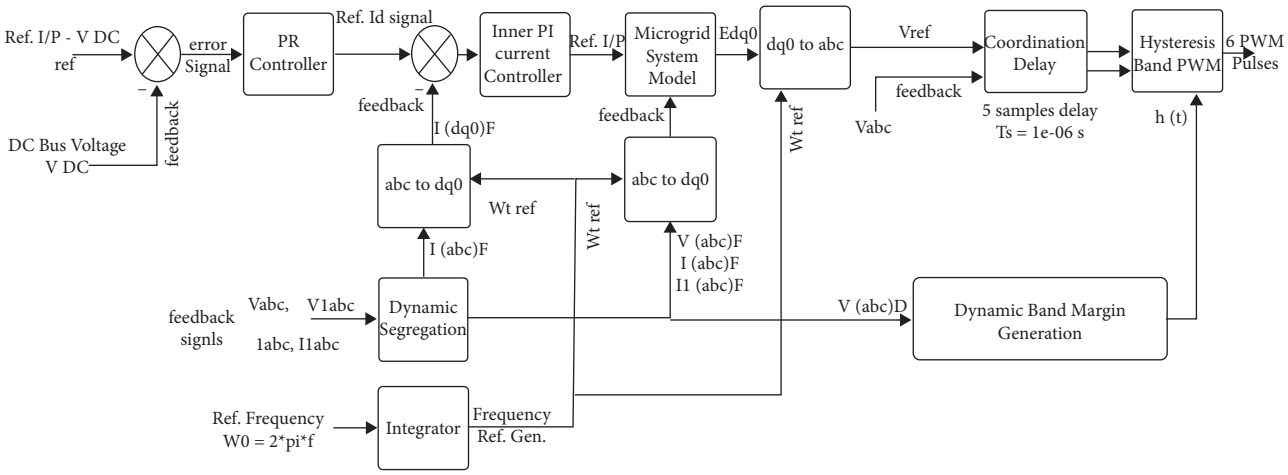

Figure 5: Schematic design of proposed SBIC-based main inverter controller.

converter, where V2G is a discharging, closed-loop boost operation control and G2V is a charging, closed-loop buck operation control, with internal current control, schematic design of which is shown in Figure 3.

The closed-loop control is described in (13)-(14). Voltage relations for V2G and G2V operations are given in (15)-(16). In (12), PI controller in discrete domain is denoted as PI.

$$\begin{aligned} \mathrm{PI}[z] &= k_p + \frac{k_i T_s}{Z-1}, \\ \mathrm{PI}[n] &= \left(\frac{1}{2\pi j}\right)\left\{\mathrm{PI}[z] * z^{n-1}\right\}\mathrm{d}z, \end{aligned} \tag{12}$$

$$D_1[n] = \mathrm{PI}[n] \circledast \left(\mathrm{PI}[n] \circledast \left\{V_{\mathrm{ev,ref}} - V_1\right\} - i\right), \tag{13}$$

$$D_2[n] = \mathrm{PI}[n] \circledast \left(\mathrm{PI}[n] \circledast \left\{V_{\mathrm{DC,ref}} - V_2\right\} - I\right), \tag{14}$$

$$V_2 = \frac{V_1}{1 - D_2}, \tag{15}$$

$$V_1 = D_1 V_2. \tag{16}$$

2.2.2. Converter Design for AC Side EV System. AC side EV modules are integrated into the AC bus of MG with the help of a modified bidirectional AC ↔ DC converter design including a circulating current protection circuit within the converter. V2G discharging operation is carried out with DC ⟶ AC conversion and G2V charging operation is carried out with AC ⟶ DC conversion. This AC ⟶ DC conversion requires an uncontrolled AC ⟶ DC rectifier with a DC ⟶ DC buck converter connected in a cascaded manner. The schematic design of the proposed AC ↔ DC bidirectional converter with its control is shown in Figure 4. Circulating current protection circuit logic is given in (17)–(20).

$$S_1 = 1\,(\mathrm{on}) \forall I_2 = 0, \tag{17}$$

$$S_1 = 0\,(\mathrm{off}) \forall I_2 \neq 0, \tag{18}$$

$$S_2 = 1\,(\mathrm{on}) \forall I_1 = 0, \tag{19}$$

$$S_2 = 0\,(\mathrm{off}) \forall I_1 \neq 0. \tag{20}$$

PI controllers are the same as in (12).

The command or switching signals, for connection or disconnection of both DC side EV systems and AC side EV systems, are generated by the ESM scheme, which is discussed in Section 3.

3. Proposed Control Strategy

This section describes the following:

(a) Proposed novel SBIC structure for the main inverter interfacing the DC and AC bus of MG.

(b) ESM scheme for meeting the energy requirements to ensure the proper functioning of MG.

(c) Coordination among SBIC module, ESM scheme, and control module of renewable generation and EVs.

3.1. Main Inverter Controller. The proposed controller is shown in Figure 5. Inputs, given to the controller, are DC bus voltage and system frequency reference. Feedback voltage and current signals are also being supplied. PWM pulses are taken as output signals. As there is no external inertia support of power grid, LBSS, or turbine system in the MG system (Figure 1), it is essential to have a robust and self-adaptive controller design to ensure the proper functioning of MG under any kind of disturbances and with high penetration of converter interfaced RES and EV systems.

To ensure the same, dynamic segregation and dynamic band margin (DBM) generation blocks are introduced in the controller, which modifies the feedback signals before injecting them into the inner current controller (ICC) and hysteresis band PWM blocks. The novel segregation feature, which segregates the fundamental component from feedback, makes the controller robust and the DBM makes the controller self-adaptive.

A delay element is introduced in the controller for effective coordination and to avoid control lag. PR controller is used for improving the steady-state performance and space vector frame transformation is used to reduce the complexity of the control structure.

A schematic of the PR controller [44] is shown in Figure 6, which is used for DC bus voltage control and the output of the PR controller is supplied to ICC as referenced-axis current i_d^* and reference q-axis current is taken as $i_q^* = 0$. The transfer function of the PR controller is given in (21), while i_d^* is expressed in (23).

$$\mathrm{PR}[z] = \frac{a\left(k_p a + k_r\right)}{a^2 + \omega_0^2}, \quad \mathrm{PR}[n] = \left(\frac{1}{2\pi j}\right)\left\{\mathrm{PR}[z] * z^{n-1}\right\}\mathrm{d}z, \tag{21}$$

$$a = \frac{z-1}{T_s}, \tag{22}$$

$$i_d^*[n] = \mathrm{PR}[n] \circledast \left(V_{\mathrm{DC,ref}} - V_{\mathrm{DC}}\right). \tag{23}$$

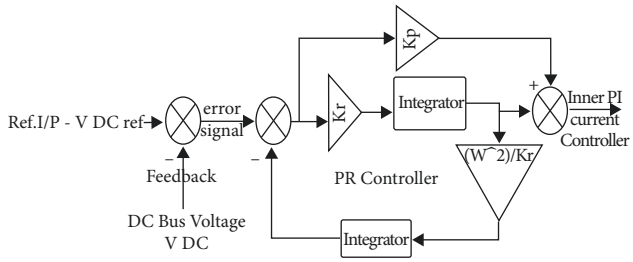

Figure 6: Schematic diagram of used PR controller.

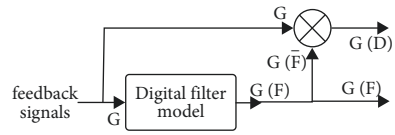

Figure 7: Schematic diagram of dynamic segregation block.

Fundamental components of feedback signals, before injecting into ICC and MG system model, are segregated, through digital filter operations, as shown in Figure 7. This segregation is used to achieve coordination among high bandwidth PR controller output signals, low bandwidth feedback signals, and dynamics of high bandwidth PI controller, same as (12), used in ICC.

For any given signal G, this can be expressed as

$$G = G(F) + G(D). \tag{24}$$

The digital filter model used to segregate the fundamental $G(F)$ is as follows.

Consider a discrete form of signal G as $G[n]$, which is formulated as (25).

$$G[n] = y_0 e^{-(n/N)} + y_1 * \sin\left(\frac{2\pi n}{N} + \theta_1\right) + y_3 * \sin\left(\frac{6\pi n}{N} + \theta_3\right), \tag{25}$$

$$e^{-(n/N)} = \left(1 - \frac{n}{N} + \frac{n^2}{2N^2} - \frac{n^3}{6N^3} + \cdots\right), \tag{26}$$

$$\begin{aligned} k_n &= \frac{2\pi n}{N}, \\ y_{1c} &= y_1 \cos\,\theta_1, \\ y_{1s} &= y_1 \sin\,\theta_1. \end{aligned} \tag{27}$$

Using (27),

$$\begin{aligned} y_1 * \sin\left(\frac{2\pi n}{N} + \theta_1\right) &= y_1 * [\sin(k_n)\cos\,\theta_1 + \cos(k_n)\sin\,\theta_1] \\ &= y_{1c}\sin(k_n) + y_{1s}\cos(k_n). \end{aligned} \tag{28}$$

Substituting (26) and (28) in (25) yields

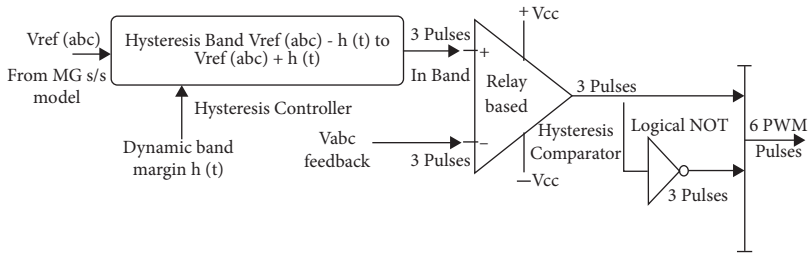

Figure 8: Schematic diagram of hysteresis controller.

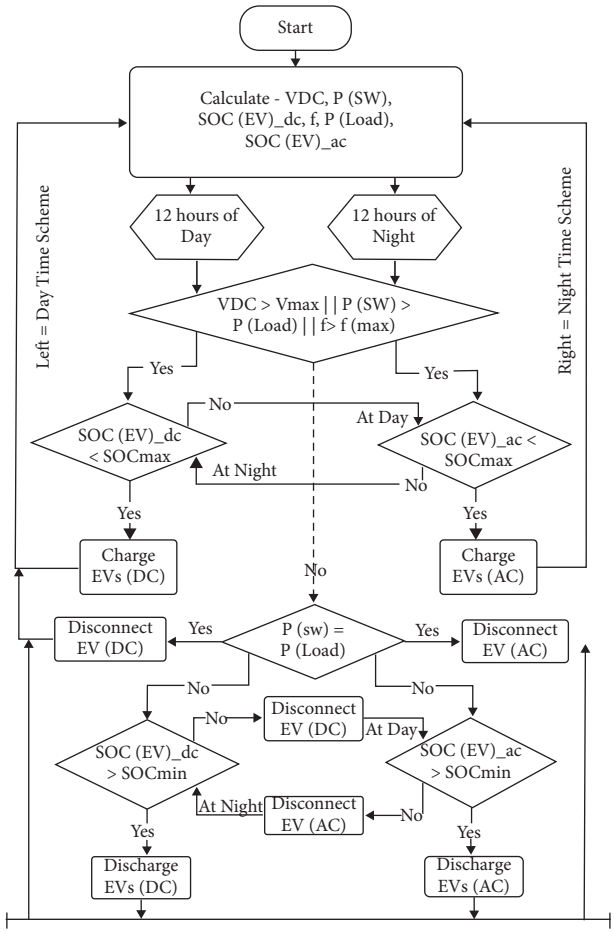

Figure 9: Flowchart of energy storage management scheme.

$$G[n] = y_0\left(1 - \frac{n}{N} + \frac{n^2}{2N^2} - \frac{n^3}{6N^3}\right) + y_{1c}\sin(k_n) + y_{1s}\cos(k_n) + y_{3c}\sin(3k_n) + y_{3s}\cos(3k_n), \tag{29}$$

$$\left(1 - \frac{n}{N} + \frac{n^2}{2N^2} - \frac{n^3}{6N^3}\right) = j_n. \tag{30}$$

Table 1: System parameters.

Parameter	Value
$V_{DC,ref}$	600 V
f	50 Hz
V_{ACL-L}	400 V
f_{min}	48.5 Hz
f_{max}	51.5 Hz
V_{min}	570 V
V_{max}	630 V
f_{sw}	50 kHz
S_{ref}	1000 W/m^2
T_{ref}	25°C
$V_{oc-boost}$	363 V
C_{boost}	3.267 mF
L_{boost}	1.43 mH
$P_{solar-rated}$	100 kW
$P_{wind-rated}$	30 kW
u_{wind}	12 m/s
H_t	4
K_s	0.3
D_t	1
SOC_{min}	40%
SOC_{max}	95%
L	500 μH
C	100 μF
R	0.02Ω

Having $n = 1, 2, 3, \ldots, N$ samples, $y_0, y_{1c}, y_{1s}, y_{3c}, y_{3s}$ are computed from the following matrix.

$$\begin{bmatrix} G[1] \\ G[2] \\ \cdots \\ G[N] \end{bmatrix} = \begin{bmatrix} j_1 & \sin(k_1) & \cos(k_1) & \sin(3k_1) & \cos(3k_1) \\ j_2 & \sin(k_2) & \cos(k_2) & \sin(3k_2) & \cos(3k_2) \\ \cdots & \cdots & \cdots & \cdots & \cdots \\ j_N & \sin(k_N) & \cos(k_N) & \sin(3k_N) & \cos(3k_N) \end{bmatrix} \begin{bmatrix} y_0 \\ y_{1c} \\ y_{1s} \\ y_{3c} \\ y_{3s} \end{bmatrix}. \tag{31}$$

Inversing the matrix, we get

$$\begin{bmatrix} y_0 \\ y_{1c} \\ y_{1s} \\ y_{3c} \\ y_{3s} \end{bmatrix} = \begin{bmatrix} j_1 & \sin(k_1) & \cos(k_1) & \sin(3k_1) & \cos(3k_1) \\ j_2 & \sin(k_2) & \cos(k_2) & \sin(3k_2) & \cos(3k_2) \\ \cdots & \cdots & \cdots & \cdots & \cdots \\ j_N & \sin(k_N) & \cos(k_N) & \sin(3k_N) & \cos(3k_N) \end{bmatrix}^{-1} \begin{bmatrix} G[1] \\ G[2] \\ \cdots \\ G[N] \end{bmatrix}. \tag{32}$$

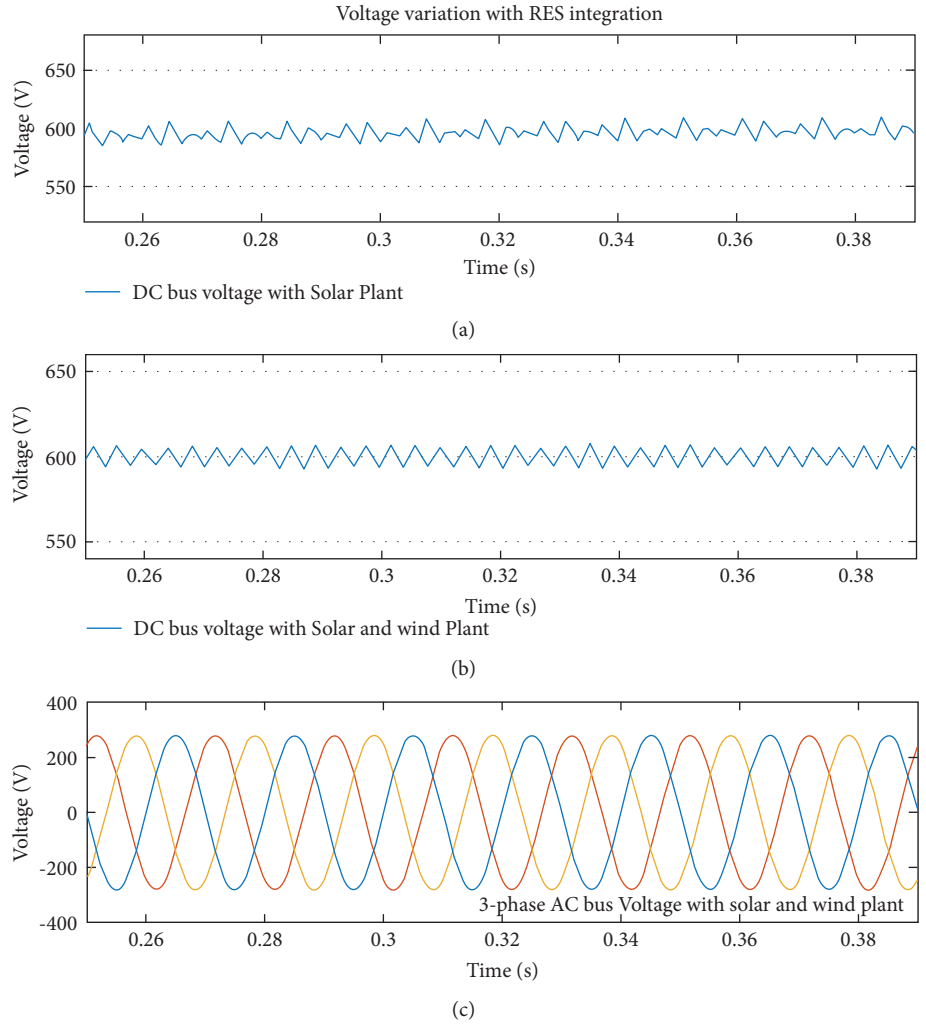

FIGURE 10: Voltage profiles. (a) DC bus voltage robustness of MG with solar plant integration. (b) DC bus voltage sensitivity of MG with both solar and wind plants. (c) Three-phase AC bus voltage of MG with solar and wind plant integrated.

From (32), the functions $G(F)[n]$ and $G(D)[n]$ can be computed as follows.

$$G(F)[n] = x[n]\sin\left(\frac{2\pi n}{N} + \delta\right) = x[n] * \left[\sin\left(\frac{2\pi n}{N}\right)\cos(\delta) + \cos\left(\frac{2\pi n}{N}\right)\sin(\delta)\right], \tag{33}$$

$$x[n]\cos(\delta) = x_c[n], \quad x[n]\sin(\delta) = x_s[n], \tag{34}$$

$$G(F)[n] = x_c[n]\sin\left(\frac{2\pi n}{N}\right) + x_s[n]\cos\left(\frac{2\pi n}{N}\right), \tag{35}$$

$$x_c[n] = \sqrt{y_{1c}^2 + \left(\frac{y_{3c}}{\sqrt{3}}\right)^2}, \tag{36}$$

$$x_s[n] = \sqrt{y_{1s}^2 + \left(\frac{y_{3s}}{\sqrt{3}}\right)^2}, \tag{37}$$

$$G(D)[n] = G[n] - G(F)[n]. \tag{38}$$

Thus, same as the above equations, feedback voltages and current signals can be segregated as given in (39)–(41) and will be supplied wherever necessary.

$$V_{abc} = V_{abc}(F) + V_{abc}(D), \tag{39}$$

$$i_{abc} = i_{abc}(F) + i_{abc}(D), \tag{40}$$

$$i1_{abc} = i1_{abc}(F) + i1_{abc}(D). \tag{41}$$

Modeling of ICC is given in (44)-(45) through frame transformation as given in (42)-(43).

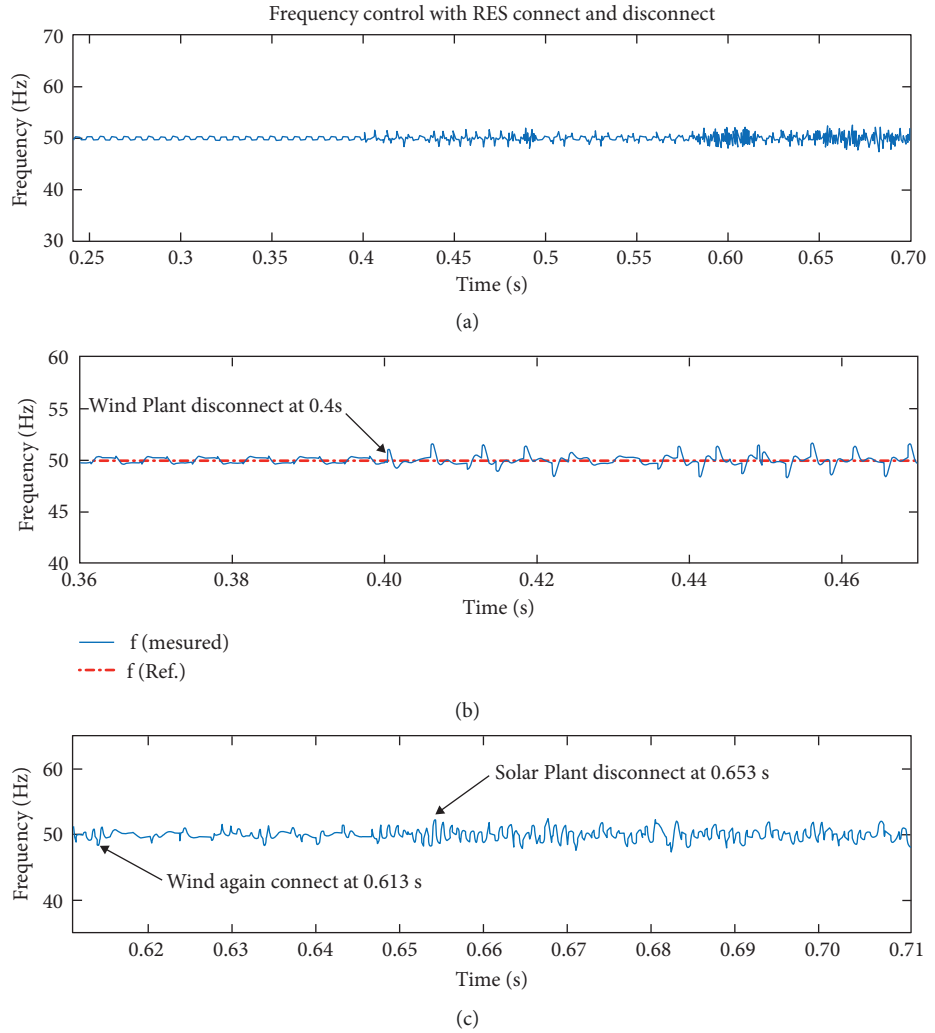

FIGURE 11: Load frequency robustness waveforms (a) shows complete time scale, (b) zoom version of (a) From $t = 0.36$ s to 0.47 s, (c) zoom version of (a) From $t = 0.61$ s to 0.71 s.

$$i_{dq\,0}(F) = [T]\left[i_{abc}(F)\right], \tag{42}$$

$$i_{dq\,0}(F) = i_d(F) + ji_q(F), \quad j = \sqrt{-1}, \tag{43}$$

$$V_d^*(F) = PI[n] \circledast \left\{i_d^*[n] - i_d(F)\right\}, \tag{44}$$

$$V_q^*(F) = -PI[n] \circledast i_q(F), \quad i_q^* = 0. \tag{45}$$

Reference inputs V_d^* and V_q^*, generated from ICC, are supplied to the MG system model which represents the LCL filter modeling as given in (48)–(50).

$$i1_{dq\,0}(F) = [T]\left[i1_{abc}(F)\right], \tag{46}$$

$$i1_{dq\,0}(F) = i1_d(F) + ji1_q(F), \tag{47}$$

$$\begin{aligned} C\frac{dV_d(F)}{dt} &= i_d(F) - i1_d(F) + \omega_0 CV_q^*(F), \\ C\frac{dV_d(F)}{dt} &= E_d, \end{aligned} \tag{48}$$

$$\begin{aligned} C\frac{dV_q(F)}{dt} &= i_q(F) - i1_q(F) - \omega_0 CV_d^*(F), \\ C\frac{dV_q(F)}{dt} &= E_q. \end{aligned} \tag{49}$$

For linear control with the fundamental component, the system satisfies the relation given in (50).

$$\frac{V_d(F)}{E_d} = \frac{V_q(F)}{E_q} = \frac{T_s}{C(z-1)}. \tag{50}$$

In the AC frame, the output of the MG system $V_{ref,abc}$ is given in (52).

$$E_d + jE_q = E_{dq\,0}, \tag{51}$$

$$V_{\text{ref},abc} = [T]^{-1}\left[E_{dq\,0}\right]. \tag{52}$$

Actual feedback V_{abc} and reference $V_{\text{ref},abc}$ are supplied to a hysteresis controller through a delay element of 5

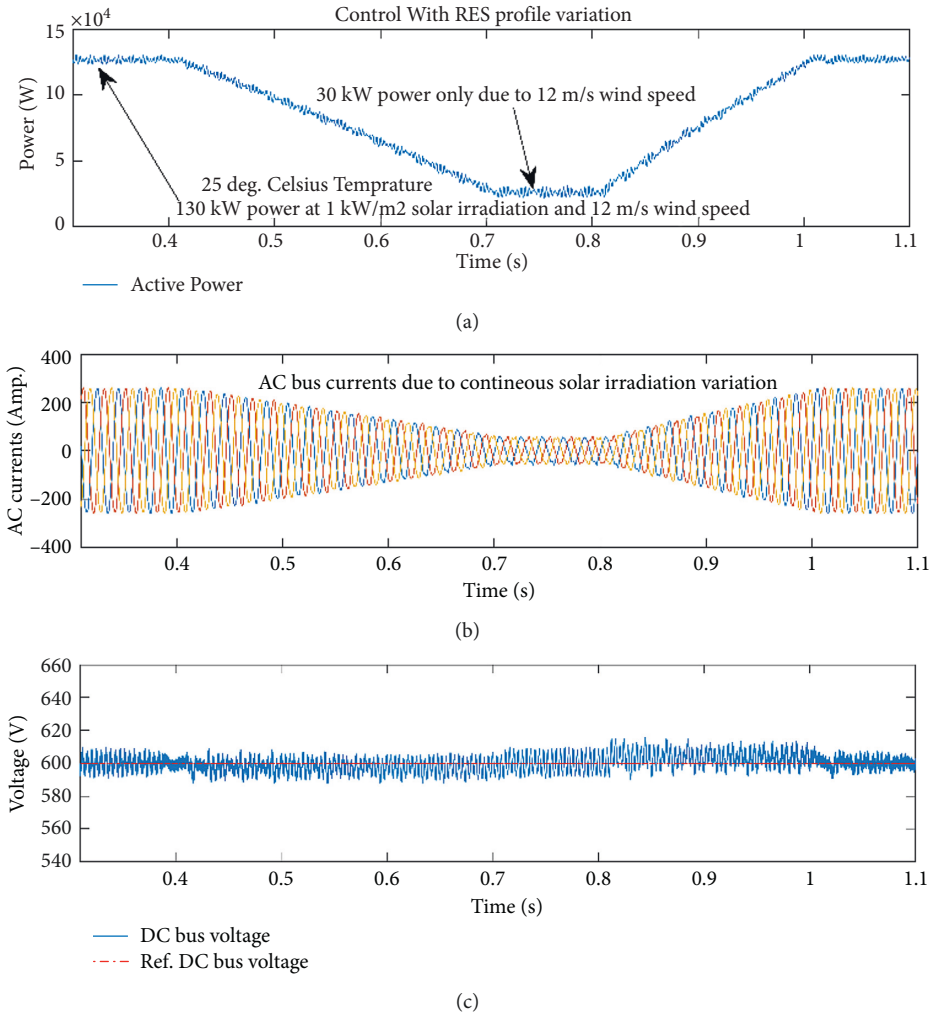

FIGURE 12: Control under continuous solar irradiation linear variation. (a) The power output at AC bus with wind plant (at base speed 12 m/s) also connected to MG. (b) The variation in AC bus three-phase currents waveforms. (c) Robustness in DC bus voltage waveform.

samples to synchronize the DBM, denoted as $h(t)$, with feedback signals and eliminate the control lag.

Dynamic band margin (DBM) is generated using feedback voltage dynamic component (anything other than a fundamental component in the signal) as evaluated in (53).

$$V_{abc}(D) = V_{abc} - V_{abc}(F). \tag{53}$$

Consecutive 5 samples of $V_{abc}(D)$ are used to generate an autovarying DBM. This varying DBM makes the hysteresis band self-changing, which makes the hysteresis controller self-adaptive. For any discrete function $f[n]$, $\text{sam}_n\{f[n]\}$ represents the consecutive 5 samples as given in

$$\text{sam}_n\{f[n]\} = \{f[n-4], f[n-3], f[n-2], f[n-1], f[n]\}. \tag{54}$$

Considering $f[n] = V_{abc}(D)$, DBM can be calculated as follows.

$$h(t) = \frac{1}{2}\left[\max\{\text{sam}_n\{V_{abc}(D)\}\} - \min\{\text{sam}_n\{V_{abc}(D)\}\}\right]. \tag{55}$$

With the above calculation, the hysteresis band will range from $V_{\text{ref},abc} - h(t)$ to $V_{\text{ref},abc} + h(t)$. The schematic diagram of the used hysteresis band-based PWM generation technique is shown in Figure 8. The detailed working of a conventional current hysteresis controller is well known as given in [45, 46].

3.2. Energy Storage Management (ESM) Scheme. The flowchart for the algorithm used in the ESM scheme, for command or signal generation for connection or disconnection of both EV systems, is given in Figure 9. ESM scheme is designed for twenty-four hours of the day. It is assumed that two separate fleets of EVs are present on the DC and AC sides, for 24 hours of the day, for energy management in the microgrid. Under the normal operating condition, wherein the supply from RES can meet the system demand, given in (69), both EV systems remain disconnected; otherwise, connection and disconnection take place according to the scheme to regulate the system parameters. The inputs given to the algorithm are P_{PV}, P_W, SOC input for both the EV modules, P_L, V_{DC}, AC bus voltage and

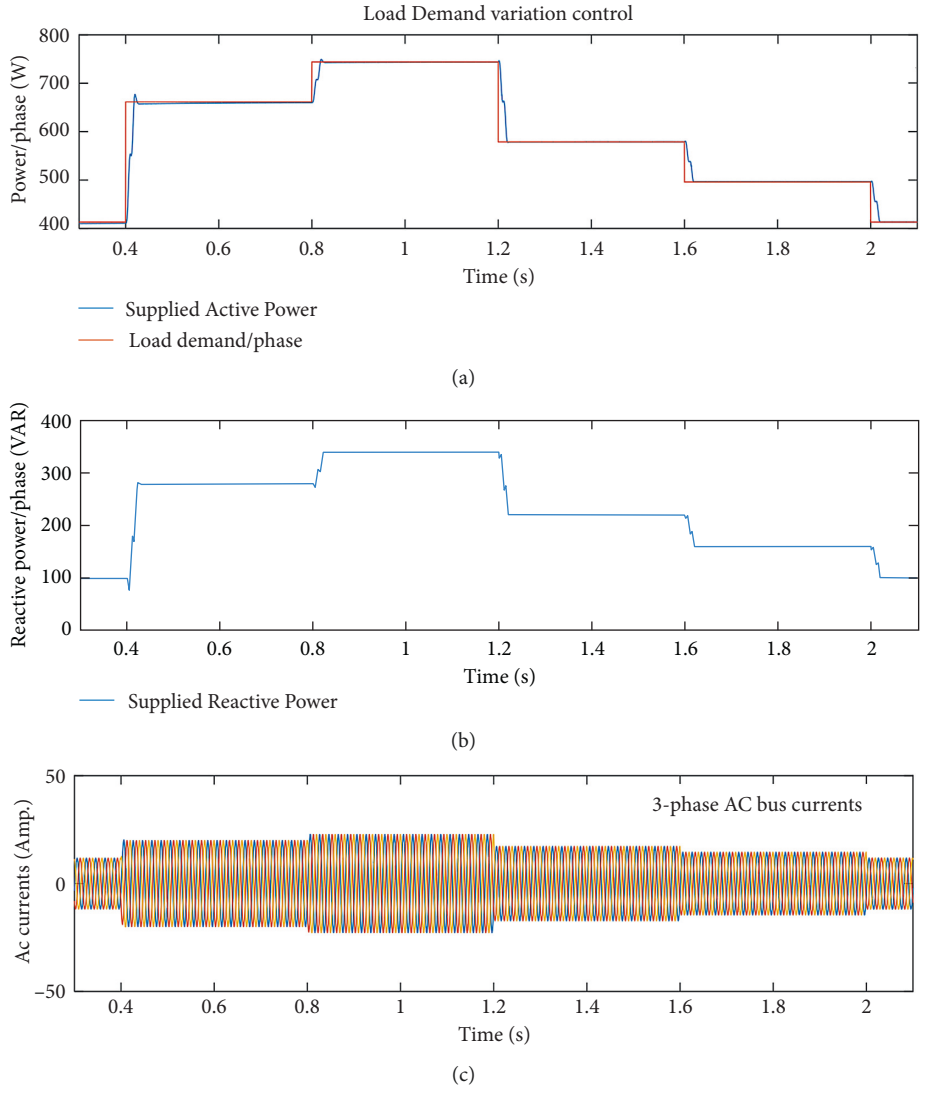

FIGURE 13: Load side power demand variations. (a) Active power per phase demand and supplied power per phase in watt. (b) Reactive power supplied/phase in VAR. (c) Three-phase AC bus currents during power demand variation.

currents, reference inputs $\mathrm{SOC}_{\min}$ and $\mathrm{SOC}_{\max}$, and $f_{\min}, f_{\max}, V_{\min}$, and $V_{\max}$.

SOC for every vehicle SOC_V present in any of EV modules must satisfy

$$\mathrm{SOC}_{\min} < \mathrm{SOC}_V < \mathrm{SOC}_{\max}. \tag{56}$$

While the connection with MG the power supplied or taken by DC and AC EV systems are $P_{\mathrm{EV,DC}}$ and $P_{\mathrm{EV,AC}}$ which are given, respectively, as follows:

$$P_{\mathrm{EV,DC}} = \sum_{i=1}^{n1} P_{iV}, \tag{57}$$

$$P_{\mathrm{EV,AC}} = \sum_{i=1}^{n2} P_{iV}. \tag{58}$$

At any time, SOC (in percentage) of any vehicle can be calculated as

$$\mathrm{SOC}_V(\%) = 100 * \left(\frac{\text{Charge present at a given time in Ah}}{\text{Rated charge of a vehicle battery in Ah}}\right). \tag{59}$$

As an indicative parameter of EV modules, the average SOC for overall modules $\mathrm{SOC}_{\mathrm{EV,DC}}$ and $\mathrm{SOC}_{\mathrm{EV,AC}}$ can be calculated as follows.

$$\mathrm{SOC}_{\mathrm{EV,DC}}(\%) = \sum_{i=1}^{n1} \frac{\mathrm{SOC}_{iV}(\%)}{n1}, \tag{60}$$

$$\mathrm{SOC}_{\mathrm{EV,AC}}(\%) = \sum_{i=1}^{n2} \frac{\mathrm{SOC}_{iV}(\%)}{n2}. \tag{61}$$

Combined RES power can be written as P_{SW}, given as

$$P_{\mathrm{SW}} = P_{\mathrm{PV}} + P_W. \tag{62}$$

Power flow management is given in (63)–(66).

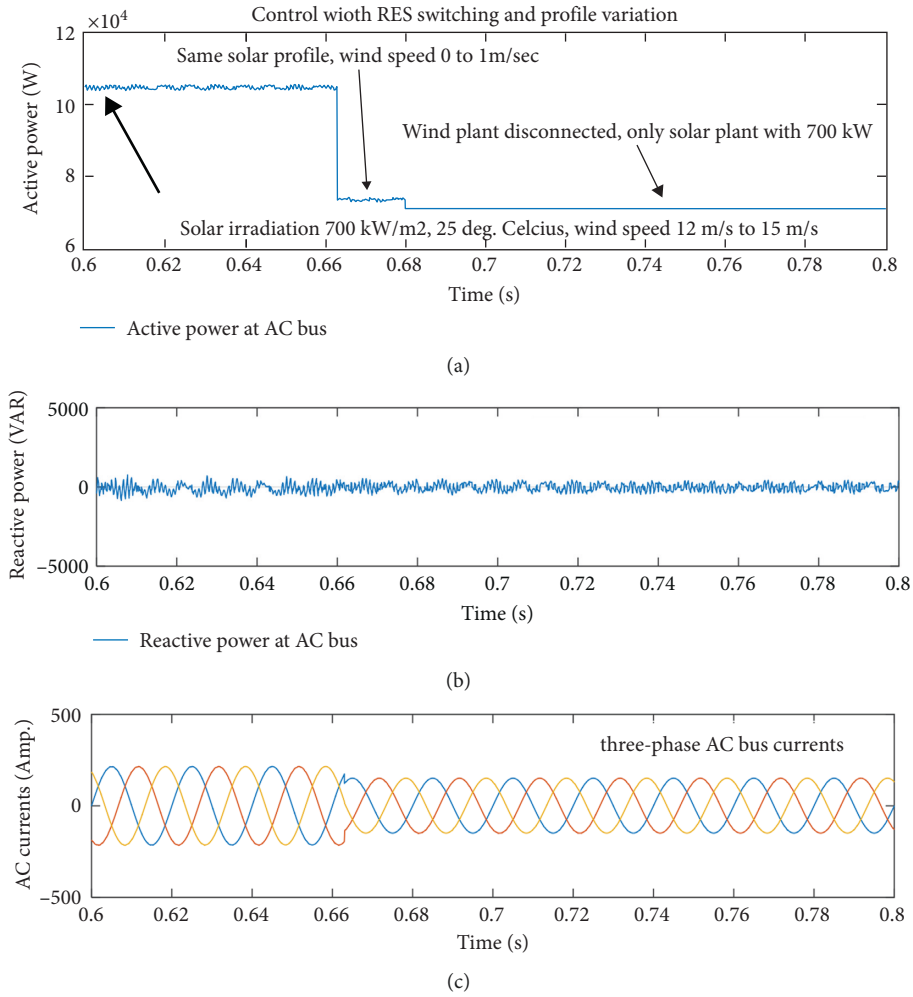

Figure 14: (a) Active power at the load bus. (b) Reactive power at the load bus. (c) Three-phase AC bus currents.

Case 1. $\mathbf{P_{SW} > P_L}$ (charging)

$$\text{Day time } P_{\text{SW}} - P_L = P_{\text{EV,DC}}, \tag{63}$$

$$\text{Night time } P_{\text{SW}} - P_L = P_{\text{EV,AC}}. \tag{64}$$

Case 2. $\mathbf{P_{SW} < P_L}$ (discharging)

$$\text{Day time } P_{\text{SW}} + P_{\text{EV,DC}} = P_L, \tag{65}$$

$$\text{Night time } P_{\text{SW}} + P_{\text{EV,AC}} = P_L. \tag{66}$$

DC bus voltage and frequency of AC bus f_{AC} must satisfy the following conditions.

$$V_{\min} < V_{\text{DC}} < V_{\max}, \tag{67}$$

$$f_{\min} < f_{\text{AC}} < f_{\max}. \tag{68}$$

The normal operating condition of MG when no EV system will be connected is given in (69) along with (67), (68).

$$P_{SW} = P_{PV} + P_W = P_L. \tag{69}$$

Extreme positive or negative case scenarios of extremely low load demand (need of generation curtailment/feed-in management) or requirement of load shedding are not considered during this study and thus not included in the ESM scheme.

3.3. Coordination among SBIC Module, ESM Scheme, and Control Module of Renewable Generation and EVs

(i) Control logic, used in renewable generation converters, is for extracting the maximum amount of power from solar and wind plants having nonlinear characteristics.

(ii) Control logic, used in EV bidirectional converters, is to maintain power flow in the right direction using the constant voltage charging method and also eliminate the risk of circulating current in the converters. Switching of EV modules (connection and disconnection from MG) is decided by the ESM scheme through digital switching signals.

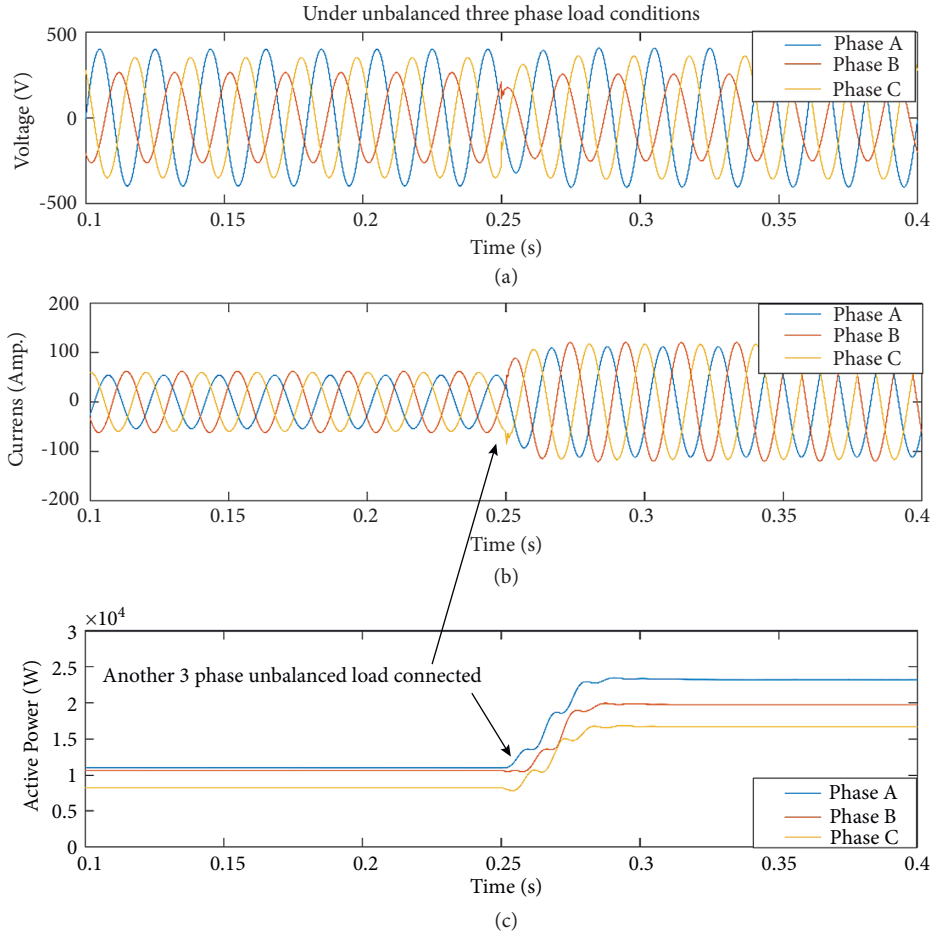

Figure 15: (a) AC bus three-phase voltages. (b) AC bus three-phase currents. (c) Active power for each phase.

(iii) ESM scheme only decides on switching of EV modules (from conditions specified in Section 3.2). EV control regulated the power flow direction but along with the fact that stabilization of MG parameters to their reference values is also essential which is being governed by the SBIC module.

(iv) First of all, renewable control deals with extracting maximum power which is continuously varying which triggers the ESM scheme to decide for connection or disconnection of EV modules. Simultaneously, SBIC control tries to stabilize the MG system. Thus, overall coordination is established among all the control modules employed in the system.

4. Simulation Results and Discussions

The proposed MG system as shown in Figure 1 is modeled in the MATLAB/SIMULINK platform. Data for load demand variation, RES profile variation are created by authors themselves. The system parameters used for simulation are shown in Table 1.

For analyzing the performance of the controller and ESM scheme, various case scenarios have been taken, which are given below.

4.1. Controller Performance and Sensitivity Analysis. To validate the performance and robustness/sensitivity of the controller under disturbances of the MG system, some cases have been considered without ESM scheme and EV integration, while maintaining the power balance between generation and demand.

4.1.1. Voltage Control with RES Integration. The solar plant is integrated with the DC bus of microgrid and the voltage of the DC bus remains well within permissible limits due to the controller as shown in Figure 10(a). When the wind plant is integrated with already having a solar plant on the DC bus, the voltage becomes more stable because of wind plant inertia aiding to DC bus of MG as shown in Figure 10(b). Three-phase AC bus voltage is shown in Figure 10(c) with solar and wind plant integrated to DC bus of MG.

4.1.2. Frequency Regulation and Robustness under Switching of RES. In the isolated microgrid, initially, both RES (solar and wind) modules are connected to the DC bus of MG. At $t = 0.4$ s, wind plant is disconnected; again at $t = 0.613$ s, wind plant is connected to the DC bus of MG, and then at $t = 0.653$ s, solar plant is disconnected from the MG. The variation in the frequency due to these switching is shown in Figure 11. The

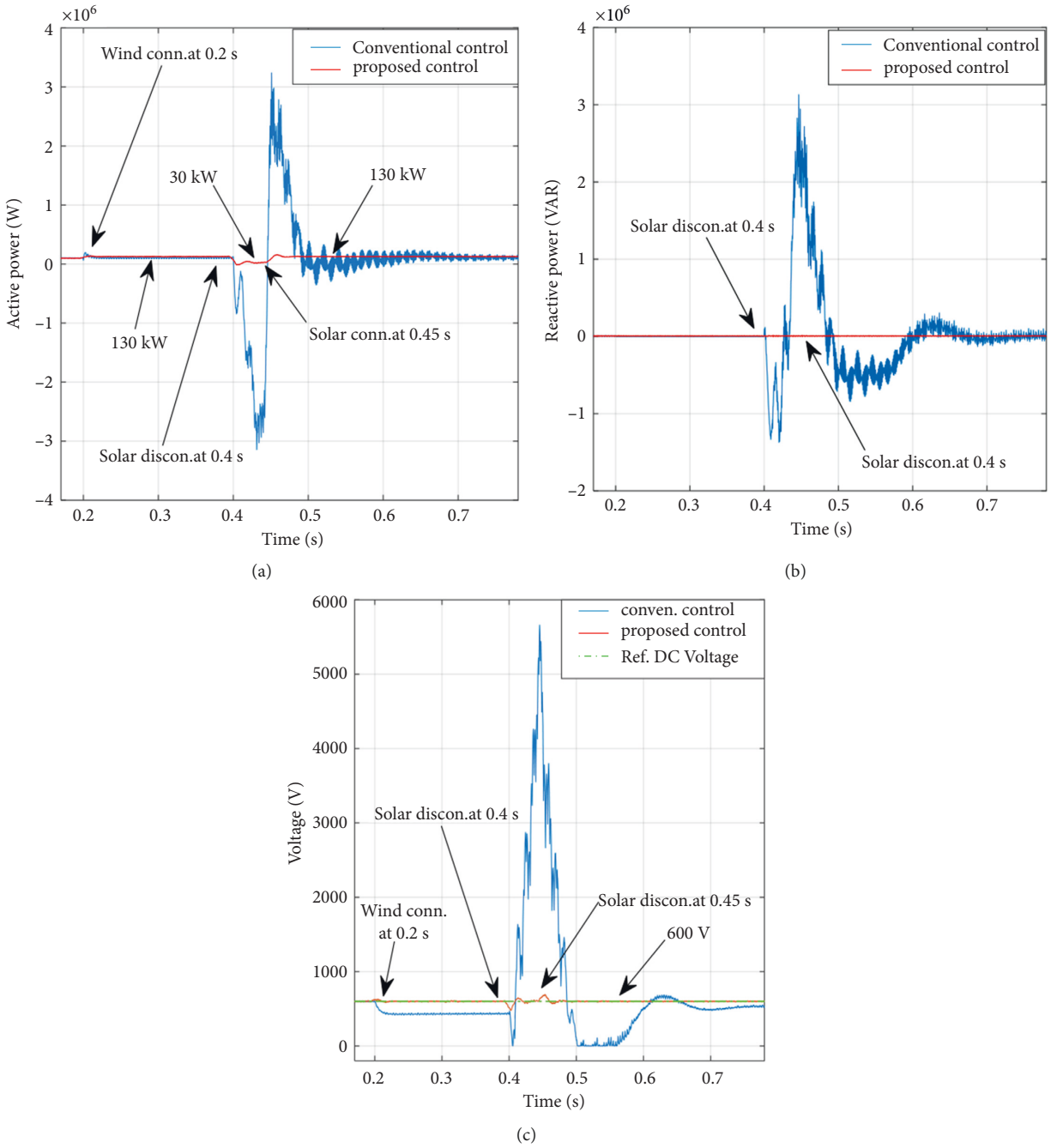

FIGURE 16: Failure of conventional control and comparison with proposed control while RES connections and disconnections. Till $t = 0.2$ s, only solar plant is supplying 100 kW of power at 600 V DC bus reference voltage; at $t = 0.2$ s, wind plant is connected, and supplied power rises to 130 kW, at $t = 0.4$ s, solar plant disconnected and again connected at $t = 0.45$ s. (a) Active power. (b) Reactive power. (c) DC bus voltage.

controller is effective in maintaining the frequency within the permissible limits specified. Variations after $t = 0.653$ s are high relative to that of $t = 0.4$ s because the major power supply to the MG was contributed by the solar plant and disconnection of the same leads to higher fluctuations; however, due to the proposed controller, frequency is regulated.

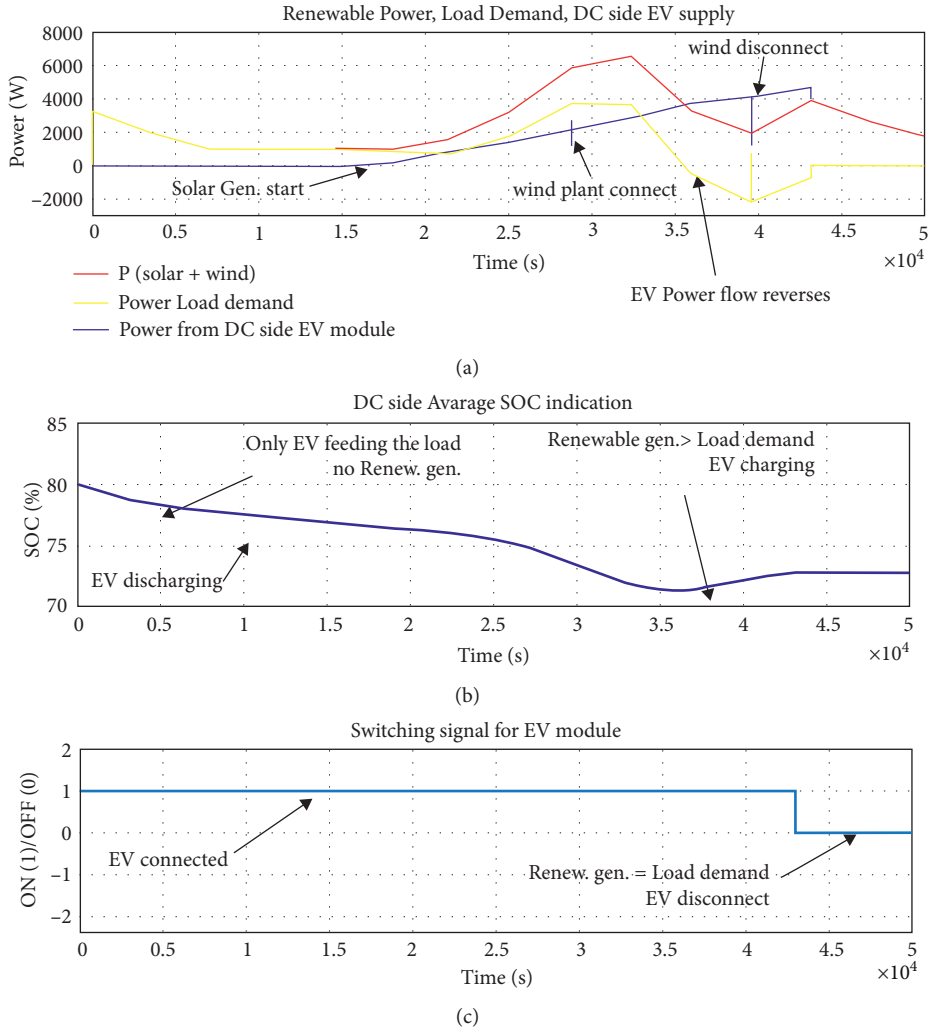

FIGURE 17: Twelve hours, daytime simulation with DC side EV module. (a) Solar and wind power generation with wind plant connect and disconnect, load power demand, and power from DC side EV module. (b) Average SOC indication parameter in percentage for DC side EV module. (c) Switching signal from ESM algorithm for DC side EV module.

4.1.3. Control and Robustness of MG System under RES Profile Variation. The solar irradiation is decreased linearly from 1 kW/m^2 to complete disconnection level from $t = 0.4$ s to 0.7 s. Further, the plant is connected back and solar irradiation is linearly increased from 0 to 1 kW/m^2 at $t = 0.8$ s to 1 s. Temperature is kept at a reference value of 25°C. The wind plant, working at a base wind speed of 12 m/s is connected to the MG. From $t = 0.7$ s to 0.8 s, only wind plant power of 30 kW is available at AC bus. The controller is effective in maintaining the sinusoidal nature of the three-phase AC bus currents and keeps the DC bus voltage within permissible limits during the variations as shown in Figure 12.

4.1.4. Control and Robustness of MG with Load Power Demand Variation. The load active power, as well as reactive power demand, is varied step-wise at $t = 0.4$ s, 0.8 s, 1.2 s, 1.6 s, and 2.0 s to check the inverter capability to sustain the load demand variation. Active power per phase demand and supplied power by the inverter, supplied reactive power per phase by inverter, and three-phase AC bus current waveforms are shown in Figure 13. The controller is effectively supplying switching signals to the inverter for sustaining disturbances.

4.1.5. Control and Robustness of MG under RES Profile Variation and Switching. Active and reactive power control is validated with large and sudden variation in wind profile and also with disconnection of wind plant completely. As shown in Figure 14, solar irradiation and temperature in this case are kept constant at 700 kW/m^2 and 25°C, respectively. Till $t = 0.663$ s, wind speed was hovering between 12 m/s to 15 m/s and the total generation was from 103 kW to 105 kW. After $t = 0.663$ s, wind speed suddenly drops down to 0 to 1 m/s and generation falls to 72 kW to 73 kW at $t = 0.68$ s; the wind plant is disconnected from the DC bus; thus, only solar generation of 70 kW is left. For these variations, active power profile is shown in Figure 14(a), reactive power profile is hovering around 0 kVAR as the load used in this case is

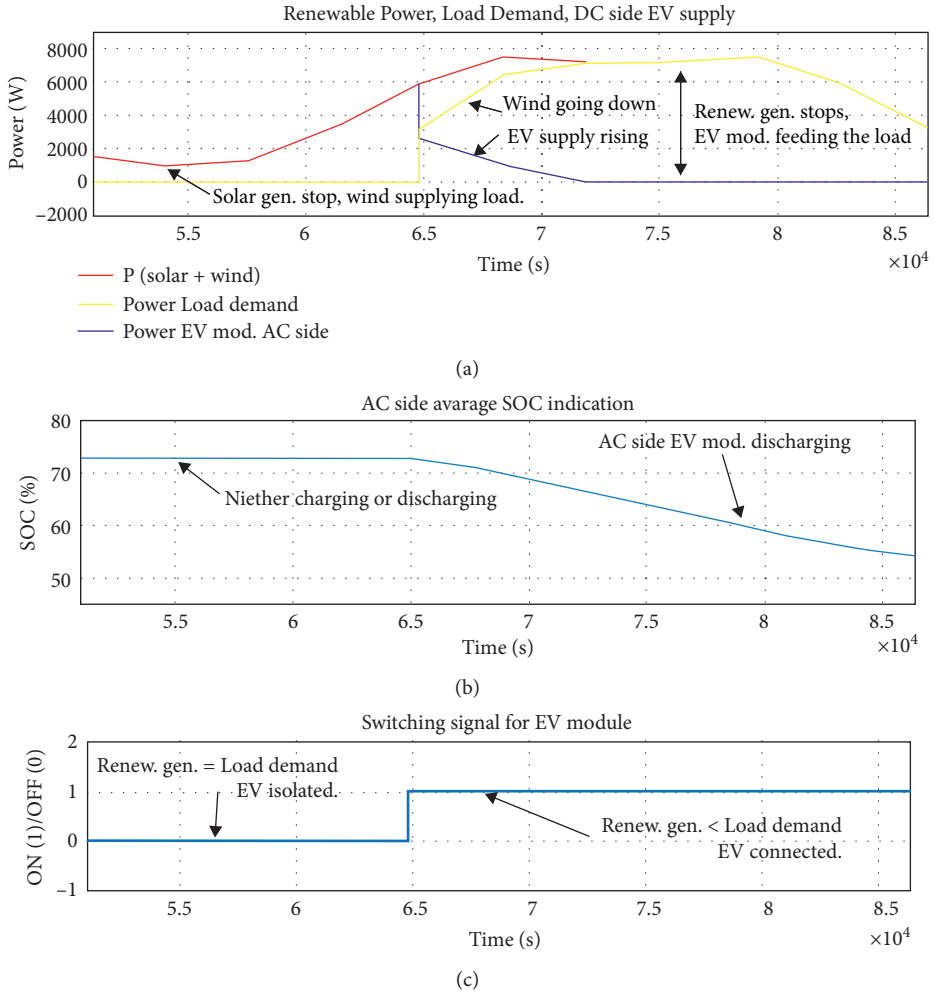

Figure 18: Twelve-hour nighttime simulation with AC side EV module. (a) Solar and wind power generation with solar plant disconnect, load power demand, and power from AC side EV module. (b) Average SOC indication parameter in percentage for AC side EV module. (c) Switching signal from ESM algorithm for AC side EV module.

purely resistive. Small fluctuations are there in the reactive power profile (Figure 14(b)) due to the filter circuit and other converters elements present in the system. Three-phase AC bus currents are shown in Figure 14(c) for the same variation.

4.1.6. Controller Robustness under Unbalanced Loading Condition. Due to the self-adaptive nature of the proposed controller, it can work with three-phase unbalanced loading conditions, and on switching extra random load, it can supply power to the system. Since unbalanced loads voltage and current magnitude of every phase are not identical but are having sinusoidal nature and on increasing the load at $t = 0.25$ s, only three-phase current rises and voltage magnitudes remain at the same level.

Initially load demand of phases A, B, and C is 10.7 kW, 10.5 kW, and 9.3 kW, respectively. At $t = 0.25$ s, another load is switched on which increases the load demand of phases A, B, and C to 21 kW, 18 kW, and 15 kW, respectively. For these variations, the three-phase AC bus voltage is shown in Figure 15(a), three-phase AC bus currents are shown in Figure 15(b), and the active power of each phase is shown in Figure 15(c).

4.1.7. Comparison with the Conventional Control Technique. While applying conventional control [4, 5, 9] in the proposed model with solar and wind plant connection and disconnection, conventional control (CC) fails to converge as reported in Figure 16. In conventional control, the DC bus voltage control is generally separated from inverter control; thus, on switching the generation plants such large spikes appear in the results while in proposed control, the control of DC bus voltage is integrated with inverter controller; thus, it can withstand the disturbances as shown in Figure 16(c). Controller, having self-adaptive nature due to the virtue of dynamic band margin, is also able to control active and reactive power while conventional control shows a very poor response as can be seen in Figures 16(a) and 16(b). Even for wind plant connection, a permanent voltage dip appears in the system with conventional control while in the proposed

control strategy MG system can withstand all kinds of RES connections and disconnections.

4.2. Performance with Energy Storage Management (ESM) Scheme. The effectiveness of the proposed ESM scheme has been tested through a few cases to check its ability to stabilize the system under switching instructions provided by the ESM algorithm and to check on any control lag due to the ESM strategy. Phasor-based simulation is performed in this case.

4.2.1. Twelve-Hour Daytime Simulation with DC Side Electric Vehicle (EV) Modules. Continuously varying RES data is considered with wind plant connection and disconnection and varying load power demands are taken with daytime consideration, and DC side EV modules, as per the ESM algorithm. DC side EV module is connected with 120 vehicles with a 500 Ah rating and charging voltage of 240 V. Results for the twelve-hour daytime (4 am to 4 pm≅50000 s) simulation have been shown in Figure 17. RES power generation with wind plant connection and disconnection, power demand by the load, power supplied or taken by the EV modules is shown in Figure 17(a). Negative values of power indicate that EVs are charging and zero power indicates the disconnection of the EV module. The indication parameter of the average SOC of the module (59) is shown in Figure 17(b). It can be easily seen SOC of EV modules is well within the range specified. A negative slope indicates that the EV module is discharging, the positive slope for charging, and no slope for isolation. The switching signal from the ESM algorithm is shown in Figure 17(c). Value 1 specifies connection and 0 specifies disconnection. The proposed control technique is in good coordination with the ESM scheme.

4.2.2. Twelve-Hour Nighttime Simulation with AC Side Electric Vehicle (EV) Module. While considering nighttime (4p.m. to 4a.m.≅45000 s) simulation solar plant disconnection is considered, and continuously varying generation and load demand are considered. AC side EV modules are integrated and controlled with the ESM algorithm. In the EV module, 210 vehicles are considered with a 500 Ah rating and charging voltage of 240 V. The complete formulation is shown in Figure 18. RG power output, solar disconnection, wind generation decrement, load demand which is dynamically supplied by both RES and EV module, and power flow from AC side EV modules are shown in Figure 18(a). The average SOC indication parameter which shows isolation or discharging is shown in Figure 18(b). The average SOC of the overall module is well within specified limits during the nighttime. Switching signals for connection or disconnection of AC side EV module from ESM scheme are shown in Figure 18(c). Value 1 specifies connection and 0 specifies disconnection. The proposed control technique is in good coordination with the ESM scheme without any control lag.

5. Conclusion

In this article, a control scheme for an islanded microgrid, which is independent of centralized storage, external inertia support, and relying only on distributed EV-based storage for ESM, is proposed. The proposed control scheme is free from iterative computational algorithms; thus, it occupies relatively less memory, produces no control lag, and is free from being stuck at local optimum operation. Intrinsic mechanisms and nonlinearities of interfacing power electronic converters are also considered in the system while designing the control as shown in Section 2.2.

The proposed scheme incorporates a novel self-adaptive discrete sample type segregation-based inverter control structure, which generates dynamic band margin, integrated with a voltage hysteresis controller and a proportional-resonant controller. The proposed scheme establishes a proper orchestration among the main control module, ESM module, and RES, EVs converter control module as given in Section 4.2. The proposed controller is robust against load variation, unbalanced loading, renewable energy uncertainties, and RES switching as shown in Section 4.1. This scheme, while RES switching, shows way better performance than conventional PI controller, as can be seen in Figure 16. The system retains its performance intact in the whole range from rated solar irradiation to plant completely cut off from the system and also from rated wind speed to wind plant cutoff from microgrid thus highly robust against input parameter variation as shown during sensitivity analysis in Figures 12 and 14.

As a future directive, a small hydro and fuel cell-based renewable generation can be integrated to test the coordination between the control scheme and ESM module (a complex and advanced design will be required) under multiple power generation modules for optimized power flow in the system.

Nomenclature

(1) Solar plant

j_1, j_2, j_3: Thermal and irradiation constants

$P(j), P(j), V_j, I_j$: Power difference, power, voltage, and current at jth sample

n, k, j: Total number of samples, the sample of maximum power, and sample count

$L_{\text{boost}}, C_{\text{boost}}$: Solar boost converter inductance and capacitance

$P_{\text{solar-rated}}$: Solar output power

$V_{\text{oc-boost}}$: Open-circuit solar panel voltage or input of boost converter

f_{sw}: Switching frequency of boost converter

(2) Wind plant

H_t, K_s, D_t: Inertia constant, shaft stiffness, and damping coefficient

ω_{es}, θ_{sa}: Base electrical speed and shaft twist angle

ω, ω_r: Angular velocity of wind turbine and permanent magnet synchronous generator

T_m, T_s: Wind mechanical torque and generator shaft torque

(3) DC and AC side electric vehicle system

$V_{\text{ev,ref}}$, $V_{\text{DC,ref}}$: Reference voltages of electric vehicle module and DC bus of microgrid

D_1, D_2: The duty cycle for buck and boost operation

V_1, V_2: Measured voltages of electric vehicle module and DC bus of microgrid

S_1, S_2: Switching signals for protection switches of DC-AC and AC-DC conversion circuits

i, I: Measured currents of electric vehicle module and DC bus of microgrid

(4) Control parameters

k_p, k_i, k_r: Proportional, integral, and resonant constants

$i_{dq\,0}, i1_{dq\,0}, V_{dq\,0}, V1_{dq\,0}$: Feedback currents and voltages of sub-AC bus and AC bus in dq 0 frame

T_s, Z: Sample time of the system and Z-transform parameter in the discrete domain

$i_d, i_q, i1_d, i1_q, V_d, V_q, V1_d, V1_q$: Feedback currents and voltages of sub-AC bus and AC bus in d-axis and q-axis of dq 0frame

abc, dq 0: Three-phase AC frame and rotational time-invariant DC frame

$V_{abc}(F), V1_{abc}(F)$, $i_{abc}(F), i1_{abc}(F)$, $V_{dq\,0}(F), V1_{dq\,0}(F)$, $i_{dq\,0}(F), i1_{dq\,0}(F)$: Fundamental components of feedback voltages and currents in abc and dq 0 frame:

$[T], [T]^{-1}$: Transformation matrices from abc to dq 0 frame and dq 0 to abc frame

$V_{abc}(D), V1_{abc}(D)$, $i_{abc}(D), i1_{abc}(D)$, $V_{dq\,0}(D), V1_{dq\,0}(D)$, $i_{dq\,0}(D), i1_{dq\,0}(D)$: Dynamic components of feedback voltages and currents in abc and dq 0 frame

ω_0, f: Reference angular frequency and given nominal frequency

$i_d(F), i_q(F), i1_d(F)$, $i1_q(F), V_d(F), V_q(F)$, $V1_d(F), V1_q(F)$: Fundamental components of currents and voltages in d-axis and q-axis of dq 0 frame

V_{DC}: Feedback DC bus voltage

$E_d, E_q, E_{dq\,0}, V_{\text{ref},abc}$: Output voltages of microgrid system model in d-axis, q-axis, in dq 0 frame, and abc frame

$V_{abc}, V1_{abc}$: Feedback voltages of sub-AC bus and AC bus in abc frame

$h(t)$: Dynamic band margin of hysteresis controller

$i_{abc}, i1_{abc}$: Feedback currents of sub-AC bus and AC bus in abc frame

$\text{sam}_n V_{abc}(D)$: Array of five samples of $V_{abc}(D)$ from $(n-4)$th sample to current nth sample

L, C: LCL filter inductance and capacitance

V_{ACL-L}: Nominal RMS line to line AC bus voltage

(5) Energy storage management scheme parameters

$V_{\min}, V_{\max}$: Minimum and maximum permissible limits of DC bus voltage

f_{AC}: Measured frequency of AC bus of microgrid

$P_{\text{EV,DC}}$, $P_{\text{EV,AC}}$: Net power supplied or consumed by DC and AC side vehicle system modules

$f_{\min}, f_{\max}$: Minimum and maximum permissible limits of AC bus frequency

P_{iV}: Power of ith vehicle attached either of DC or AC side vehicle module

P_{PV}, P_W, P_L: Instantaneous power of the solar plant, wind plant, and load demand

$\text{SOC}_{\min}$, $\text{SOC}_{\max}$: Minimum and maximum permissible limits of vehicle state of charge

P_{SW}: Instantaneous power of solar and wind plant

SOC_{iV}: Measured state of charge for ith vehicle

$\text{SOC}_{\text{EV,DC}}$, $\text{SOC}_{\text{EV,AC}}$: State of charge indication parameters for DC and AC side vehicle module.

Data Availability

The data used to support the findings of this study are included in the article.

Conflicts of Interest

The authors declare that they have no conflicts of interest regarding the publication of this paper.

References

[1] C. J. Mozina, "Impact of green power distributed generation," *IEEE Industry Applications Magazine*, vol. 16, no. 4, pp. 55–62, 2010.

[2] O. Singh, A. Iqbal, S. Kumar, and S. Rajput, "Hybrid renewable energy system integration in the micro-grid: Indian context," in *Proceedings of the International Conference on Control, Computing, Communication and Materials (ICCCCM)*, pp. 1–5, Allahabad, India, October 2016.

[3] L. Ahmethodzic and Mustafa Music, "Comprehensive review of trends in microgrid control," *Renewable Energy Focus*, vol. 38, pp. 84–96, 2021.

[4] L. Fan, "Frequency and voltage control in microgrids," in *Control and Dynamics in Power System and Microgrids*, pp. 147–169, CRC Press, New York, NY, USA, 1st edition, 2017.

[5] E. Kabalci, H. Irgan, and Y. Kabalci, "Hybrid microgrid system design with renewable energy sources," in *Proceedings of the 2018 IEEE 18th International Power Electronics and Motion Control Conference (PEMC)*, pp. 387–392, Budapest, Hungary, August 2018.

[6] T. Kerdphol, S. R. Fathin, W. Masayuki et al., "Enhanced virtual inertia control based on derivative technique to emulate simultaneous inertia and damping properties for microgrid frequency regulation," *IEEE Access*, vol. 7, pp. 14422–14433, 2019.

[7] X. Hou, Y. Sun, Z. Xin, J. H. Lu, W. Peng, and M. G. Josep, "Improvement of frequency regulation in VSG-based AC microgrid via adaptive virtual inertia," *IEEE Transactions on Power Electronics*, vol. 35, no. 2, pp. 1589–1602, 2020.

[8] A. Tavakoli, S. Saha, M. T. Arif, E. Haque, M. Nishad, and M. T. Aman, "Impacts of grid integration of solar PV and electric vehicle on grid stability, power quality and energy economics: a review," *IET Energy Systems Integration*, vol. 2, no. 3, pp. 243–260, 2020.

[9] J. Rocabert, A. Luna, B. Frede, and R. Pedro, "Control of power converters in AC microgrids," *IEEE Transactions on Power Electronics*, vol. 27, no. 11, pp. 4734–4749, 2012.

[10] K.-W. Lao, W. Y. Deng, J. P. Shang, and N. Dai, "PQ-coupling strategy for droop control in grid-connected capacitive-coupled inverter," *IEEE Access*, vol. 7, pp. 31663–31671, 2019.

[11] T. Wu, G. Bao, Y. Y. Chen, and J. P. Shang, "A review for control strategies in microgrid," in *Proceedings of the 2018 37th Chinese Control Conference (CCC)*, pp. 30–35, Wuhan, China, July 2018.

[12] J. Wang, A. Pratt, and M. Baggu, "Integrated synchronization control of grid-forming inverters for smooth microgrid transition," in *Proceedings of the IEEE Power and Energy Society General Meeting (PESGM)*, pp. 1–5, Atlanta, GA, USA, August 2019.

[13] Z. Liu, J. Liu, and Y. Zhao, "A unified control strategy for three-phase inverter in distributed generation," *IEEE Transactions on Power Electronics*, vol. 29, no. 3, pp. 1176–1191, 2014.

[14] M. E. Haque, M. Negnevitsky, and K. M. Muttaqi, "A novel control strategy for a variable-speed wind turbine with a permanent-magnet synchronous generator," *IEEE Transactions on Industry Applications*, vol. 46, no. 1, pp. 331–339, 2010.

[15] T. Rashid, A. Routh, R. Rana, A. Ferdous, and R. Sayed, "A novel approach to maximize performance and reliability of PMSG based wind turbine: Bangladesh perspective," *American Journal of Engineering Research (AJER)*, vol. 7, no. 6, pp. 17–26, 2018.

[16] N. Thodsaporn and V. Kinnares, "Wind turbine simulator equipped with real-time monitoring and user-friendly parameter setup controlled by C2000 microcontroller," in *Proceedings of the 2020 17th International Conference on Electrical Engineering/Electronics, Computer, Telecommunications and Information Technology (ECTI-CON)*, pp. 713–716, Phuket, Thailand, June 2020.

[17] Z. Gao, J. Li, M. Zhao, C. Zhou, and L. Kai, "Design and simulation of 500 kw wind-solar complementary microgrid," in *Proceedings of the 2020 Chinese Control and Decision Conference (CCDC)*, pp. 5499–5505, Hefei, China, August 2020.

[18] P. S. Kumar, R. P. S. Chandrasena, V. Ramu, G. N. Srinivas, and K. V. S. M. Babu, "Energy management system for small scale hybrid wind solar battery based microgrid," *IEEE Access*, vol. 8, pp. 8336–8345, 2020.

[19] Y. Varetsky, V. Konoval, M. Saheda, and P. Olena, "Studying voltage fluctuations in microgrid with hybrid renewable energy system," in *Proceedings of the IEEE 6th International Conference on Energy Smart Systems (ESS)*, pp. 239–242, Kyiv, Ukraine, April 2019.

[20] M. Jafari, M. Zahra, J. Zhu, and M. K. Hassan, "A novel predictive fuzzy logic-based energy management system for grid-connected and off-grid operation of residential smart microgrids," *IEEE Journal of Emerging and Selected Topics in Power Electronics*, vol. 8, no. 2, pp. 1391–1404, 2020.

[21] M. Jafari, Z. Malekjamshidi, and J. Zhu, "A magnetically coupled multi-port, multi-operation-mode micro-grid with a predictive dynamic programming-based energy management for residential applications," *International Journal of Electrical Power and Energy Systems*, vol. 104, no. 1, pp. 784–796, 2019.

[22] A. Khan, S. Memon, and T. P. Sattar, "Analyzing integrated renewable energy and smart-grid systems to improve voltage quality and harmonic distortion losses at electric-vehicle charging stations," *IEEE Access*, vol. 6, pp. 26404–26415, 2018.

[23] A. Hassouneet, M. Khafallah, A. Mesbahi, and T. Bouragba, "Power management strategies of electric vehicle charging station based grid tied PV-battery system," *International Journal of Renewable Energy Resources*, vol. 8, no. 2, pp. 851–860, 2018.

[24] A. Hassouneet, M. Khafallah, A. Mesbahi, and T. Bouragba, "Improved control strategies of electric vehicles charging station based on grid tied PV/battery system," *International Journal of Advanced Computer Science and Applications*, vol. 11, no. 3, pp. 116–124, 2020.

[25] A. Hassouneet, M. Khafallah, A. Mesbahi, and T. Bouragba, "Experimental analysis of control in electric vehicle charging station based grid tied photovoltaic-battery system," *International Journal of Electrical and Computer Engineering*, vol. 13, no. 5, pp. 276–284, 2019.

[26] S. Singh, S. Jagota, and M. Singh, "Energy management and voltage stabilization in an islanded microgrid through an electric vehicle charging station," *Sustainable Cities and Society*, vol. 41, pp. 679–694, 2018.

[27] A. Hassouneet, K. Mohamed, A. Mesbahi, N. Ayoub, and B. Tarik, "Experimental implementation of a smart battery charger for electric vehicles charging station," *International Journal of Power Electronics and Drive Systems*, vol. 11, no. 4, pp. 1689–1699, 2020.

[28] S. Iqbal, M. U. Jan, X. Ai et al., "V2G strategy for primary frequency control of an industrial microgrid considering the charging station operator," *Electronics*, vol. 9, no. 4, pp. 549–570, 2020.

[29] K. Sayed, A. G. Abo-Khalil, and A. S. Alghamdi, "Optimum resilient operation and control dc microgrid based electric vehicles charging station powered by renewable energy sources," *Energies*, vol. 12, no. 22, pp. 4240–4263, 2019.

[30] E. K. Belal, D. M. Yehia, and A. M. Azny, "Adaptive droop control for balancing SOC estimation of distributed batteries in DC microgrids," *IET Generation, Transmission and Distribution*, vol. 13, no. 20, pp. 4667–4676, 2019.

[31] M. U. Jan, X. Ai, A. A. Mohamed, U. R. Haseeb, and S. Iqbal, "Adaptive and fuzzy PI controllers design for frequency regulation of isolated microgrid integrated with electric vehicles," *IEEE Access*, vol. 8, pp. 87621–87632, 2020.

[32] H. Karimi, T. Mohammad, H. Beheshti, R. Amin, and H. Zareipour, "Intelligent control of islanded AC microgrids based on adaptive neuro-fuzzy inference system," *International Journal of Electrical Power and Energy Systems*, vol. 133, Article ID 107161, 2021.

[33] J. Hu, Y. Shan, J. M. Guerrero, I. Adrian, K. W. Chan, and J. Rodriguez, "Model predictive control of microgrids—an overview," *Renewable and Sustainable Energy Reviews*, vol. 136, Article ID 110422, 2021.

[34] P. Jampeethong and S. Khomfoi, "Coordinated control of electric vehicles and renewable energy sources for frequency regulation in microgrids," *IEEE Access*, vol. 8, pp. 141967–141976, 2020.

[35] S. Ranjan, A. Latif, D. C. Das, and N. Sinha, "LFC for autonomous hybrid micro grid system of 3 unequal renewable areas using mine blast algorithm," *International Journal of Renewable Energy Resources*, vol. 8, no. 3, pp. 1297–1308, 2018.

[36] A. Latif, D. C. Das, K. B. Amar, and S. Ranjan, "Maiden coordinated load frequency control strategy for ST-AWEC-GEC-BDDG-based independent three-area interconnected microgrid system with the combined effect of diverse energy storage and DC link using BOA-optimised PFOID controller," *IET Renewable Power Generation*, vol. 13, no. 14, pp. 2634–2646, 2019.

[37] A. Latif, D. C. Das, K. B. Amar, and S. Ranjan, "Illustration of demand response supported coordinated system performance evaluation of YSGA optimized dual stage PIFOD-(1 + PI) controller employed with wind-tidal-biodiesel based independent two-area interconnected microgrid system," *IET Renewable Power Generation*, vol. 14, no. 6, pp. 1074–1086, 2020.

[38] K. V. Hessam, F. D. Mohammadi, V. Verma, J. Solanki, and S. K. Solanki, "Hierarchical multi-agent based frequency and voltage control for a microgrid power system," *International Journal of Electrical Power and Energy Systems*, vol. 135, Article ID 107535, 2022.

[39] M. U. Jan, A. Xin, H. U. Rehman, M. A. Abdelbaky, S. Iqbal, and M. Aurangzeb, "Frequency regulation of an isolated microgrid with electric vehicles and energy storage system integration using adaptive and model predictive controllers," *IEEE Access*, vol. 9, pp. 14958–14970, 2021.

[40] A. K. Barik and D. C. Das, "Coordinated regulation of voltage and load frequency in demand response supported bio-renewable cogeneration-based isolated hybrid microgrid with quasi-oppositional selfish herd optimisation," *International Transactions on Electrical Energy Systems*, vol. 30, Article ID e12176, 2020.

[41] R. Mandal and K. Chatterjee, "Frequency control and sensitivity analysis of an isolated microgrid incorporating fuel cell and diverse distributed energy sources," *International Journal of Hydrogen Energy*, vol. 45, no. 23, pp. 13009–13024, 2020.

[42] T. UttamraoSolanke, V. K. Ramachandaramurthy, Y. Y. Jia, J. Pasupuleti, P. Kasinathan, and A. Rajagopalan, "A review of strategic charging-discharging control of grid-connected electric vehicles," *Journal of Energy Storage*, vol. 28, Article ID 101193, 2020.

[43] N. Sujitha and S. Krithiga, "Grid tied PV-electric vehicle battery charger using bidirectional converter," *International Journal of Renewable Energy Resources*, vol. 9, no. 4, pp. 1873–1881, 2019.

[44] A. R. Dash, B. C. Babu, K. B. Mohanty, and D. Rahul, "Analysis of PI and PR controllers for distributed power generation system under unbalanced grid faults," in *Proceedings of the International Conference on Power and Energy Systems*, pp. 1–6, Chennai India, December 2011.

[45] H. Mao, X. Yang, Z. Chen, and Z. Wang, "A hysteresis current controller for single phase three level voltage source inverters," *IEEE Transactions on Power Electronics*, vol. 27, no. 7, 2012.

[46] P. A. Dahono, "New hysteresis current controller for single phase full bridge inverter," *IET Power Electronics*, vol. 2, no. 5, pp. 585–594, 2009.